Petroleum Science 18 (2021) 1776–1787

Contents lists available at ScienceDirect

Petroleum Science

journal homepage: www.keaipublishing.com/en/journals/petroleum-science

Original Paper

An analytical model for water-oil two-phase flow in inorganic nanopores in shale oil reservoirs

Ran Li [a], Zhangxin Chen [a, b, *], Keliu Wu [a, b, **], Xing Hao [c], Jinze Xu [a]

[a] Department of Chemical and Petroleum Engineering, University of Calgary, Calgary, Alberta, T2N 1N4, Canada
[b] State Key Laboratory of Petroleum Resources and Prospecting, China University of Petroleum, Beijing, 102249, China
[c] Illinois Institute of Technology, Chicago, IL, 60616, United States

ARTICLE INFO

Article history:
Received 22 April 2020
Accepted 28 June 2021
Available online 2 September 2021

Edited by Yan-Hua Sun

Keywords:
Shale oil
Water films
Two-phase flow
Nanopore

ABSTRACT

The existence of water phase occupies oil flow area and impacts the confined oil flow behavior at the solid substrate in inorganic nanopores of shale oil reservoirs, resulting in a completely different flow pattern when compared with the single oil phase flow. This study proposes an analytical model to describe the water-oil two-phase flow. In this model, water slippage at the solid substrate is considered while oil slip is introduced to calculate the oil movement at the solid-oil boundary in dry conditions. It is proven that the oil flow profiles of both the two-phase model and single-phase model show parabolic shapes, but the oil flow capacity drops when water takes up the flow space and the impact of water is more significant when the pore dimension is smaller than 30 nm. Also, the oil flow velocity at a pore center is found to drop linearly given a larger water saturation in wet conditions. The effects of surface wettability and oil properties on water-oil flow are also discussed. Compared with the existing single-phase models, this model describes oil flow pattern in the wet condition with the incorporation of the influence of nanopore properties, which better predicts the oil transport in actual reservoir conditions. Water-oil relative permeability curves are also obtained to improve oil yield.

1. Introduction

Shale oil is the oil reserved in shale rocks, which usually contain inorganic matrix and kerogen (Cane, 1976; Youngquist, 1998; Passey et al., 2010; Curtis et al., 2011; Afsharpoor and Javadpour, 2018). Shale rocks are dominated by micropores (<100 nm) to macropores (>1000 nm), and therefore, characterized by low porosity and low permeability (Rouquerol et al., 1994; Loucks et al., 2009; Chalmers et al., 2012; Zou, 2017; Dembicki, 2016). Nanopores tend to bring about molecular interactions between solid walls and fluid molecules near pore surfaces, which cannot be neglected in modeling the fluid transport. In this way, the fluid transport behavior in an interfacial region deviates from that of the bulk phase (Barrat and Bocquet, 1999; Holt et al., 2006; Darabi et al., 2012; Afsharpoor and Javadpour, 2016; Jin and Firoozabadi, 2016). Therefore, the confined fluids movement in shale oil reservoirs need to be investigated.

In terms of single oil phase flow in nanopores in shale reservoirs, molecular dynamics simulations (MDS) and analytical models are most frequently used methods. Wang et al. (2016a) adopted MDS to capture how *n*-octane molecules moved in inorganic nanopores with their size to be 1.7–11.2 nm. They found that the liquid hydrocarbon molecules were liable to be arranged parallel to a solid surface, the structure of which was difficult to form if the pore size became larger. Liquid slip and apparent viscosity were then chosen to describe this specific phenomenon. To compare, they also tested the single oil phase flow in organic pores. Different from the parabolic shape in inorganic pores, the velocity profile in organic pores presented a plug shape (Wang et al., 2016b). Zhang et al. (2017b) derived an analytical apparent viscosity model to calculate the oil transport with the consideration of liquid adsorption and liquid slip depending on rock wettability, and sensitivity analysis was conducted by changing pore size, pressure gradient and total organic carbon (TOC). Sun et al. (2019) also derived a single oil flow model analytically with incorporations of oil slip and

* Corresponding author. Department of Chemical and Petroleum Engineering, University of Calgary, Calgary, Alberta, T2N 1N4, Canada.
** Corresponding author. Department of Chemical and Petroleum Engineering, University of Calgary, Calgary, Alberta, T2N 1N4, Canada.
E-mail addresses: zhachen@ucalgary.ca (Z. Chen), kwu@cup.edu.cn (K. Wu).

https://doi.org/10.1016/j.petsci.2021.09.005

physical adsorption mechanisms.

However, the mentioned studies only focused on the single oil flow in shale oil reservoirs. Water-oil two-phase flow patterns in nanopores should also be analyzed as it is the prerequisite for obtaining water-oil relative permeability curves and further predicting multiphase flow rates and production. Ojha et al. (2017) developed a workflow to estimate shale relative permeability curves with low-pressure nitrogen adsorption-desorption isotherm. They concluded that a drop in water relative permeability was quicker than an increase in oil relative permeability given a small water saturation. Cantisano et al. (2013) used a Lattice-Boltzmann method to compute water-oil relative permeability curves for Colombian rocks with different wettability. Similarly, Huang et al. (2020) found water-oil and oil-gas relative permeability curves for mixed-wet shale oil reservoirs. Yu et al. (2014) obtained water-oil relative permeability curves by history matching the production data of a Middle Bakken well.

Most of the published water-oil two-phase flows in shale reservoirs are not studied with analytical models. This study provides an analytical model to compare confined oil flow capacities in both dry and wet conditions. For the dry condition, only oil slippage is introduced for the single oil phase flow. But in terms of the wet condition, both water slippage and modified water properties are considered for water films in the vicinity of a solid wall. Water-oil relative permeability curves and different fluid flow profiles can be derived in this way. Comparing the two results tells how water impacts oil transport capacity in nanoscale water-wet pores as both oil-wet and water-wet nanopores have been discovered in shale oil reservoirs (Odusina et al., 2011; Saraji and Piri, 2015; Gupta et al., 2018; Siddiqui et al., 2018; Gao et al., 2019).

2. Model establishment

As the pore size in shale oil reservoirs lies in the range of several to several thousand nanometers, solid-liquid molecular interactions are particularly significant even compared with liquid-liquid molecular interactions, which cannot be ignored in nanoscale confined structures. How oil slippage and water slippage are represented analytically is firstly discussed in this section. Then a specific model for calculating water-oil two-phase flow rates and relative permeability curves is described and derived in details. Oil adsorption at a solid surface is not considered currently, which will be considered in the future. Also, this study focuses on obtaining water-oil flow properties with an analytical model. Molecular dynamics will be conducted in the next stage to further validate the model.

2.1. Liquid slippage

The liquid slippage was proposed by Navier et al. (1823), who put forward the possibility of liquid slip on a solid surface and defined a constant slip length to measure it. In their study, a slip length was determined as the distance from a solid surface to the location where the liquid velocity was extrapolated to zero.

$$v_{ls} = l_{ls}\frac{\partial u}{\partial z} \tag{1}$$

where v_{ls} is the liquid slip velocity, m/s; l_{ls} is the liquid slip length, m; u is the liquid flow velocity, m/s; z is the direction perpendicular to the flow direction.

A liquid slip length is then frequently adopted to measure liquid slippage, and influencing factors on the liquid slip length are discussed with numerous models. According to Ruckenstein and Rajora (1983), a liquid slip velocity was proportional to a chemical potential gradient and a mobility coefficient. The mobility coefficient was further derived to be a function of a surface diffusion coefficient. The slip velocity v_{ls} and the liquid slip length l_{ls} are expressed as:

$$v_{ls} = \frac{D}{n_L k_B T}\frac{\Delta P}{L} \tag{2}$$

$$l_{ls} = \frac{2\mu D}{n_L k_B T r} \tag{3}$$

where D is a surface diffusion coeffcient, m^2/s; n_L is the liquid particle number density, dimensionless; k_B is the Boltzmann constant, 1.381×10^{-23} J/K; T is temperature, K; ΔP is a pressure difference between the ends of capillary, Pa; L is the capillary length, m; μ is a viscosity coefficient, Pa·s; r is the capillary radius, m. On the basis of Ruckenstein and Rajora's theory (1983), Mattia and Calabrò (2012) explained that the difference between solid-liquid molecular interactions and liquid-liquid molecular interactions led to the unexpected higher water flow rate in carbon nanotubes. Maintaining that $n_L k_B TL$ was the energy of fluid molecules in an interfacial region and the energy could be replaced by the work of adhesion W_A, they defined the slip velocity by Eq. (4) and the slip length was further derived as in Eq. (5). With the help of Myers's flow rate model (Myers, 2011), they successfully captured water flow characteristics in carbon nanotubes measuring different sizes and wettability.

$$v_{ls} = \frac{D}{W_A}\Delta P \tag{4}$$

$$l_{ls} = \frac{2\mu DL}{W_A r} \tag{5}$$

where W_A is the work of adhesion, J/m^2. In this way, Cui et al. (2017) analyzed oil flow in confined organic nanopores accounting for oil slippage and adsorption. They used Eqs. (4) and (5) to calculate the related slip properties, which are also used in this study to conduct analysis and discussion in the next section.

However, Blake (1990) developed a liquid slip model involving interfacial wettability on the basis of the molecular-kinetic theory in another way. He defined a slip length as the ratio of a viscosity coefficient and a slip coefficient, which was closely related to a contact angle and an effective area occupied by solid molecules.

$$\lambda_s = \frac{\mu}{\delta\left[e^{\frac{\alpha S\sigma_l(1-\cos\theta)}{k_B T}} - 1\right]} \tag{6}$$

where λ_s is a slip coefficient, Pa·s/m; δ is the distance between the two neighboring molecules, m; α is the fraction of an effective surface area occupied by solid, dimensionless; S is an effective surface area, m^2; σ_l is the liquid-solid tension, N/m; θ is a contact angle, degree. Then the liquid slip length l_{ls} is manifested as

$$l_{ls} = \delta\left[e^{\frac{\alpha S\sigma_l(1-\cos\theta)}{k_B T}} - 1\right] \tag{7}$$

During the above process, Blake (1990) ignored the difference of relaxation time between fist-layer molecules and bulk molecules. However, Wu et al. (2019) introduced this difference and studied confined n-alkane flow behavior. Therefore, Eq. (7) is modified to

$$l_{ls} = \delta\left[\frac{\tau_0}{\tau_b}e^{\frac{\alpha S\sigma_l(1-\cos\theta)}{k_B T}} - 1\right] \tag{8}$$

where τ_0 is the bulk molecules relaxation time, s; τ_b is the first layer molecules relaxation time, s. On the basis of Eq. (8), Wu et al. (2019)

plotted oil true slippage length of different alkanes as a function of wall energy and a pore diameter, which are used in the next section to discuss the impacts of *n*-alkane properties on the confined two-phase flow.

Oil slippage length l_{os} is calculated according to Eqs. (5) and (8) when single oil phase exists. In terms of water-oil two phase flow, the water slippage l_{ws} is represented with the derived model of Myers (2011). He has validated the empirical model against numerous MDS data and experimental data.

$$l_{ws} = h_{wi}\left(\frac{\mu_{wi}}{\mu_{w0}} - 1\right)\left[1 - \frac{3}{2}\frac{h_{wi}}{r_c} + \left(\frac{h_{wi}}{r_c}\right)^2 - \frac{1}{4}\left(\frac{h_{wi}}{r_c}\right)^3\right] \tag{9}$$

where l_{ws} is a water slip length, m; r_c is the pore radius, m; h_{wi} and h_{w0} are the thicknesses of two water layers, m; μ_{wi} and μ_{w0} are the water viscosity for the two water films, Pa·s, which can be calculated according to the empirical model of Qin and Buehler (2015) (Eq. (10)), who obtained the model based on classical Stokes' law with molecular forces analysis.

$$\frac{\mu_{wi}}{\mu_{w0}} = \left(C_1 + C_2 L_0^{-6}\right) \tag{10}$$

where C_1 and C_2 are constants, dimensionless; L_0 is the distance between two neighboring atoms, m.

2.2. Model derivation

Water in nano-sized hydrophilic pores tends to spread at a solid surface and occupy oil flow path as in Fig. 1. It is assumed that the water stays between a rock surface and an oil zone. And the water film is distributed uniformly at the solid surface. Only oil and water phases are considered in the current study. In the case of wet condition, the water molecules in the vicinity of solid wall have specific flow properties due to the solid-liquid molecular interactions, which are different from other bulk water molecules staying far away from the surface. In the case of hydrophilic nanopores, the water molecules near the substrate tend to have a larger viscosity. Therefore, there are two water films at the surface of a circular pore in Fig. 1 (Li et al., 2018, 2019). Water slippage is considered at a solid-water boundary during water-oil two-phase flow. In contrast, oil slippage is taken into account at the solid-oil boundary in a dry condition.

Also, it is assumed that the fluids flow laminarly in a steady-state condition, which is frequently adopted in the fluid flow study in shale pores. For example, Zhang et al. (2017a) and Li et al. (2016) assumed steady-state shale gas-water phase flow in nanopores and further derived gas-water relative permeability curves. Cui et al. (2017) assumed single-phase oil flow in a steady-state condition and liquid permeability of organic nanopores. The transient flow and pseudo-steady state flow and the phase transition between oil and gas phases will be discussed in the future study.

As one of the practical applications, this analytical model can be acted as the inputs for reservoir simulation and well test to better improve shale oil recovery. Also, the steady-state relative permeability curves are frequently used as the inputs in the commercial reservoir simulator such as CMG (CMG, 2017) and well test software such as Fekete (2017).

According to the assumed flow model, the expression for multiphase flow in the oil region and two water regions are (Chen et al., 2006)

$$\begin{cases} \dfrac{\mu_o}{r}\dfrac{\partial}{\partial r}\left(r\dfrac{\partial v_o}{\partial r}\right) = \dfrac{\partial P}{\partial x},\ r\in[0,\ r_c - h_{wi} - h_{w0}] \\ \dfrac{\mu_{w0}}{r}\dfrac{\partial}{\partial r}\left(r\dfrac{\partial v_{w0}}{\partial r}\right) = \dfrac{\partial P}{\partial x},\ r\in[r_c - h_{wi} - h_{w0},\ r_c - h_{wi}] \\ \dfrac{\mu_{wi}}{r}\dfrac{\partial}{\partial r}\left(r\dfrac{\partial v_{wi}}{\partial r}\right) = \dfrac{\partial P}{\partial x},\ r\in[r_c - h_{wi},\ r_c] \end{cases} \tag{11}$$

where P is the pore pressure, Pa; v_o is the oil velocity, m/s; v_{wi} and v_{w0} are the water velocity for two water regions, m/s; μ_o is the oil viscosity, Pa·s. In this study, μ_{wi} is equal to $C\mu_{w0}$ and C is a constant related to pore wettability.

On the basis of the previous discussion, oil slippage l_{os} is introduced to simulate the solid-oil molecular interactions at the pore inner surface when only oil phase exists. Water slippage l_{ws} is used instead if water saturation is larger than 0. The boundary conditions in this case are listed as

$$\begin{cases} \left(\dfrac{\partial v_o}{\partial r}\right)|_{r=0} = 0 \\ v_o|_{r=r_c-h_{wi}-h_{w0}} = v_{w0}|_{r=r_c-h_{wi}-h_{w0}} - l_{os}\left(\dfrac{\partial v_o}{\partial r}\right)|_{r=r_c-h_{wi}-h_{w0}} \\ \mu_o\left(\dfrac{\partial v_o}{\partial r}\right)|_{r=r_c-h_{wi}-h_{w0}} = \mu_{w0}\left(\dfrac{\partial v_{w0}}{\partial r}\right)|_{r=r_c-h_{wi}-h_{w0}} \\ v_{w0}|_{r=r_c-h_{wi}} = v_{wi}|_{r=r_c-h_{wi}} \\ \mu_{w0}\left(\dfrac{\partial v_{w0}}{\partial r}\right)|_{r=r_c-h_{wi}} = \mu_{wi}\left(\dfrac{\partial v_{wi}}{\partial r}\right)|_{r=r_c-h_{wi}} \\ v_{wi}|_{r=r_c} = -l_{ws}\dfrac{\partial v_{wh}}{\partial r}|_{r=r_c} \end{cases} \tag{12}$$

Solving Eq. (11) according to the boundary conditions in Eq. (12) obtains the following flow velocities

where L is the circular pore length, m. When water exists,

$$\begin{cases} v_o = -\dfrac{\Delta P}{4\mu_o L}r^2 + \dfrac{\Delta P h_{w0}}{4\mu_{w0}L}(2r_c - 2h_{wi} - h_{w0}) + \dfrac{\Delta P}{4\mu_{wi}L}\left(2r_c l_{ws} - {h_{wi}}^2 + 2r_c h_{wi}\right) \\ \quad + l_{os}\dfrac{\Delta P}{2\mu_o L}(r_c - h_{wi} - h_{w0}) + \dfrac{\Delta P}{4\mu_o L}(r_c - h_{wi} - h_{w0})^2 \\ v_{w0} = -\dfrac{\Delta P}{4\mu_{w0}L}r^2 + \dfrac{\Delta P}{4\mu_{w0}L}(r_c - h_{wi})^2 + \dfrac{\Delta P}{4\mu_{wi}L}\left(2r_c l_{ws} - {h_{wi}}^2 + 2r_c h_{wi}\right) \\ v_{wi} = -\dfrac{\Delta P}{4\mu_{wi}L}r^2 + \dfrac{\Delta P}{4\mu_{wi}L}{r_c}^2 + l_{ws}\dfrac{\Delta P}{2\mu_{wi}L}r_c \end{cases} \tag{13}$$

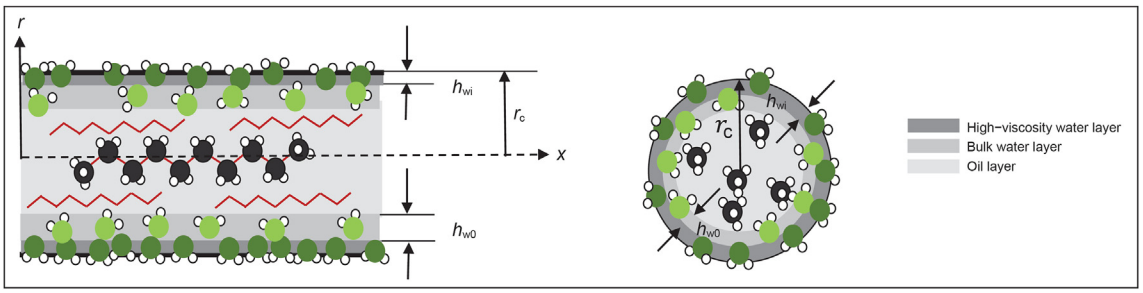

Fig. 1. Distribution of water and oil phases in a single nanopore (Oxygen in water and carbon in oil are green spheres and black spheres, respectively).

$l_{ws} = h_{wi}\left(\frac{\mu_{wi}}{\mu_{w0}}-1\right)\left[1-\frac{3}{2}\frac{h_{wi}}{r_c}+\left(\frac{h_{wi}}{r_c}\right)^2-\frac{1}{4}\left(\frac{h_{wi}}{r_c}\right)^3\right]$ and $l_{os} = 0$; when only the oil phase is present, $l_{ws} = 0$, $h_{wi} = h_{w0} = 0$, and $l_{os} = \frac{2\mu_o D_s L}{W_A r_c}$ or $l_{os} = \delta\left[\frac{\tau_0}{\tau_b}e^{\frac{\alpha S\sigma_1(1-\cos\theta)}{k_B T}}-1\right]$.

Even though this study aims to compare the flow velocity profiles, relative permeability curves are calculated to conduct model validation. The single pore flow rate equations are thus derived by integrating Eq. (13) along the r axis:

$$\begin{aligned} q_o &= 2\pi\int_0^{r_c-h_{wi}-h_{w0}} r v_o \mathrm{d}r \\ &= \frac{\pi\Delta P}{8\mu_o L}(r_c-h_{wi}-h_{w0})^4 + l_{os}\frac{\pi\Delta P}{2\mu_o L}(r_c-h_{wi}-h_{w0})^3 \\ &\quad + \frac{\pi\Delta P h_{w0}}{4\mu_{w0}L}(2r_c-2h_{wi}-h_{w0})(r_c-h_{wi}-h_{w0})^2 \\ &\quad + \frac{\pi\Delta P}{4\mu_{wi}L}\left(2r_c l_{ws}-h_{wi}^2+2r_c h_{wi}\right)(r_c-h_{wi}-h_{w0})^2 \end{aligned} \tag{14}$$

$$\begin{aligned} q_{w0} &= 2\pi\int_{r_c-h_{wi}-h_{w0}}^{r_c-h_{wi}} r v_{w0}\mathrm{d}r \\ &= \frac{\pi\Delta P h_{w0}^2}{8\mu_{w0}L}(2r_c-2h_{wi}-h_{w0})^2 \\ &\quad + \frac{\pi\Delta P\left(2r_c l_{ws}-h_{wi}^2+2r_c h_{wi}\right)}{4\mu_{wi}L}h_{w0}(2r_c-2h_{wi}-h_{w0}) \end{aligned} \tag{15}$$

$$\begin{aligned} q_{wi} &= 2\pi\int_{r_c-h_{wi}}^{r_c} r v_{wi}\mathrm{d}r \\ &= \frac{\pi\Delta P h_{wi}(2r_c-h_{wi})}{8\mu_{wi}L}\left(2r_c h_{wi}-h_{wi}^2+4r_c l_{ws}\right) \end{aligned} \tag{16}$$

where q_o is the single pore oil flow rate, m^3/s; q_{wi} and q_{w0} are the single pore water flow rates for the two water regions, m^3/s.

Assuming a log-normal pore size distribution for shale oil reservoirs, the total flow rate equations are then obtained by adding the flow rates from the minimum radius r_{cmin} to the maximum radius r_{cmax} (Zhang et al., 2017a).

$$\begin{aligned} Q_{ot} = N\int_{r_{cmin}}^{r_{cmax}} &\left\{\frac{\pi\Delta P}{8\mu_o L}(r_c-h_{wi}-h_{w0})^4 + l_{os}\frac{\pi\Delta P}{2\mu_o L}(r_c-h_{wi}-h_{w0})^3\right. \\ &+\frac{\pi\Delta P h_{w0}}{4\mu_{w0}L}(2r_c-2h_{wi}-h_{w0})(r_c-h_{wi}-h_{w0})^2 \\ &\left.+\frac{\pi\Delta P}{4\mu_{wi}L}\left(2r_c l_{ws}-h_{wi}^2+2r_c h_{wi}\right)(r_c-h_{wi}-h_{w0})^2\right\} \\ &\times\frac{1}{r_c\sqrt{2\pi\sigma_{r_c}^2}}\exp\left[-\frac{(\ln r_c-\varsigma_{r_c})^2}{2\sigma_{r_c}^2}\right]\mathrm{d}r_c \end{aligned} \tag{17}$$

$$\begin{aligned} Q_{wt} = N\int_{r_{cmin}}^{r_{cmax}} &\left\{\frac{\pi\Delta P h_{w0}^2}{8\mu_{w0}L}(2r_c-2h_{wi}-h_{w0})^2\right. \\ &+\frac{\pi\Delta P\left(2r_c l_{ws}-h_{wi}^2+2r_c h_{wi}\right)}{4\mu_{wi}L}h_{w0}(2r_c-2h_{wi}-h_{w0}) \\ &\left.+\frac{\pi\Delta P h_{wi}(2r_c-h_{wi})}{8\mu_{wi}L}\left(2r_c h_{wi}-h_{wi}^2+4r_c l_{ws}\right)\right\}\frac{1}{r_c\sqrt{2\pi\sigma_{r_c}^2}} \\ &\exp\left[-\frac{(\ln r_c-\varsigma_{r_c})^2}{2\sigma_{r_c}^2}\right]\mathrm{d}r_c \end{aligned} \tag{18}$$

where N is the total number of circular pores, dimensionless; r_{cmin} and r_{cmax} are the minimum pore radius and the maximum pore radius, m; Q_{ot} is the total oil flow rate, m^3/s; Q_{wt} is the total water flow rates, m^3/s.

The Darcy flow rate of oil phase Q_{od} and the water saturation S_w take the following forms:

$$Q_{od} = \frac{K_{ot}A(1-S_w)}{\mu_o}\frac{\Delta P}{L} \tag{19}$$

$$S_w = 1 - \frac{N\int_{r_{cmin}}^{r_{cmax}}\pi(r_c-h_{wi}-h_{w0})^2\frac{1}{r_c\sqrt{2\pi\sigma_{r_c}^2}}\exp\left[-\frac{(\ln r_c-\varsigma_{r_c})^2}{2\sigma_{r_c}^2}\right]\mathrm{d}r_c}{N\int_{r_{cmin}}^{r_{cmax}}\pi r_c^2\frac{1}{r_c\sqrt{2\pi\sigma_{r_c}^2}}\exp\left[-\frac{(\ln r_c-\varsigma_{r_c})^2}{2\sigma_{r_c}^2}\right]\mathrm{d}r_c} \tag{20}$$

where Q_{od} is the Darcy flow rate of oil phase, m^3/s; A is the cross

section area, m^2; S_w is the water saturation, dimensionless.

Considering the pore tortuosity τ obtains

$$Q_{od} = \frac{1}{\tau} Q_{ot} \tag{21}$$

where τ is the pore tortuosity, dimensionless.

Substituting Eqs. (17), (18) and (20) into Eq. (21), one can get the oil apparent permeability K_{ot} during two-phase flow:

$$K_{ot} = \frac{N}{A(1-S_w)\tau}\mu_o \int_{r_{cmin}}^{r_{cmax}} \left\{ \frac{\pi}{8\mu_o}(r_c - h_{wi} - h_{w0})^4 + l_{os}\frac{\pi}{2\mu_o}(r_c - h_{wi} - h_{w0})^3 + \frac{\pi h_{w0}}{4\mu_{w0}}(2r_c - 2h_{wi} - h_{w0})(r_c - h_{wi} - h_{w0})^2 + \frac{\pi}{4\mu_{wi}}\left(2r_c l_{ws} - h_{wi}^2 + 2r_c h_{wi}\right)(r_c - h_{wi} - h_{w0})^2 \right\} \times \frac{1}{r_c\sqrt{2\pi\sigma_{r_c}^2}} \exp\left[-\frac{(\ln r_c - \varsigma_{r_c})^2}{2\sigma_{r_c}^2} \right] dr_c \tag{22}$$

where K_{ot} is the oil apparent permeability during two-phase flow, m^3.

Likewise, the water apparent permeability K_{wt} and the absolute permeability K_t when only water phase exists are derived as follows:

$$K_{wt} = \frac{N}{AS_w\tau}\mu_w \int_{r_{cmin}}^{r_{cmax}} \left\{ \frac{\pi h_{w0}^2}{8\mu_{w0}}(2r_c - 2h_{wi} - h_{w0})^2 + \frac{\pi\left(2r_c l_{ws} - h_{wi}^2 + 2r_c h_{wi}\right)}{4\mu_{wi}} h_{w0}(2r_c - 2h_{wi} - h_{w0}) + \frac{\pi h_{wi}(2r_c - h_{wi})}{8\mu_{wi}}\left(2r_c h_{wi} - h_{wi}^2 + 4r_c l_{ws}\right) \right\} \frac{1}{r_c\sqrt{2\pi\sigma_{r_c}^2}} \exp\left[-\frac{(\ln r_c - \varsigma_{r_c})^2}{2\sigma_{r_c}^2} \right] dr_c \tag{23}$$

$$K_t = \frac{N}{A\tau}K_t \int_{r_{cmin}}^{r_{cmax}} \left\{ \frac{\pi(r_c - h_{wi})^4}{8\mu_{w0}} + \frac{\pi\left(2r_c l_{ws} - h_{wi}^2 + 2r_c h_{wi}\right)}{4\mu_{wi}}(r_c - h_{wi})^2 + \frac{\pi h_{wi}(2r_c - h_{wi})}{8\mu_{wi}}\left(2r_c h_{wi} - h_{wi}^2 + 4r_c l_{ws}\right) \right\} \frac{1}{r_c\sqrt{2\pi\sigma_{r_c}^2}} \exp\left[-\frac{(\ln r_c - \varsigma_{r_c})^2}{2\sigma_{r_c}^2} \right] dr_c \tag{24}$$

where K_{wt} is the water apparent permeability during two-phase flow, m^3; K_t is the absolute permeability when only water phase exists, m^3. When water exists, $l_{ws} = h_{wi}\left(\frac{\mu_{wi}}{\mu_{w0}} - 1\right)\left[1 - \frac{3}{2}\frac{h_{wi}}{r_c} + \left(\frac{h_{wi}}{r_c}\right)^2 - \frac{1}{4}\left(\frac{h_{wi}}{r_c}\right)^3\right]$ and $l_{os} = 0$; when only the oil phase is present, $l_{ws} = 0$, $h_{wi} = h_{w0} = 0$, $l_{os} = \frac{2\mu_o D_s L}{W_A r_c}$ or $l_{os} = \delta\left[\frac{\tau_0}{\tau_b} e^{\frac{\alpha S\sigma_1(1-\cos\theta)}{k_B T}} - 1\right]$.

Finally, water-oil relative permeabilities are obtained as $k_{rw} = K_{wt}/K_t$ and $k_{ro} = K_{ot}/K_t$.

3. Model validation

The derived relative permeability model is validated against the published tight oil and shale oil relative permeability data in Fig. 2 (Yu et al., 2014; Wantawin et al., 2017; Bo et al., 2019) as the nanoscale oil apparent permeability data considering the existence of water lacks. The parameters used during validation are listed in Table 1 and the mean-squared error (MSE) measuring the validation accuracy is listed in Table 2. The deviation between experimental data and simulation results is estimated to come from the complex pore structure. The actual pore size distribution is not able to strictly follow the log-normal distribution, which is used to derive the relative permeability curves in this study.

4. Results and discussion

The two-phase velocity distribution and relative permeability curves are discussed under different conditions to evaluate the impacts of influencing factors such as pore size, water saturation, pore wettability, etc.

4.1. Velocity distribution

4.1.1. Pore size

With the basic parameters listed in Table 3 (Details are listed in Appendix), the flow velocity profile at the water saturation of 0.5 is

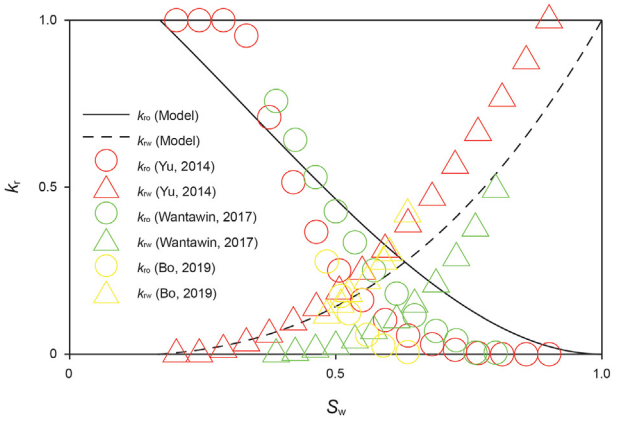

Fig. 2. Relative permeability data validation between experimental data and the derived model.

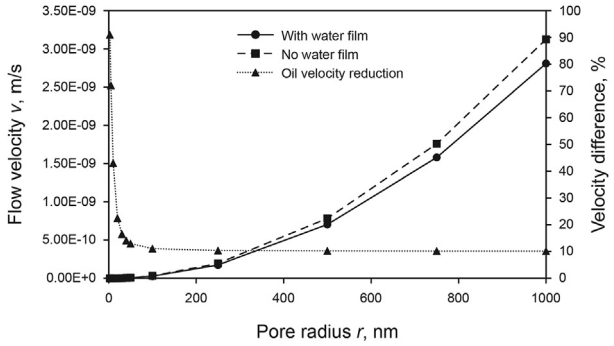

Fig. 4. Relationship between maximum oil flow velocities and pore radius (θ=81.1°, $S_w = 0.5$, $\omega = 0.577$).

shown in Fig. 3. The dimensionless radius r_D is used instead of r in this part ($r_D = r/r_0$). According to Fig. 3, the oil flow profile follows a parabolic shape both in a dry condition and a wet condition, which agrees with the MDS results of Wang et al. (2016a). But there is a turning point at the water-oil interface due to the property differences between the two phases. Also, the presence of water reduces oil flow capacity significantly. The oil flow velocity is 1.2353×10^{-13} m/s at the water-oil interface and it increases to 2.7976×10^{-13} m/s at the center when the average pore radius is 10 nm. In this case, oil slippage disappears at the interface and the minimum oil flow velocity comes from the moving water films. The minimum high-viscosity water velocity and bulk water flow velocity are calculated to be 1.6461×10^{-14} m/s and 2.8129×10^{-14} m/s, respectively. The non-zero high-viscosity water flow velocity at the substrate is the result of water slippage. In terms of the single oil phase, the maximum oil flow velocity turns out to be 4.9087×10^{-13} m/s and it drops to 1.7841×10^{-13} m/s at the solid surface, which is generated by oil movements at the pore wall. To conclude, considering the existence of movable water films brings about a reduction in oil flow capacity by 42.97% at the center. One reason goes to the occupation of an oil flow section area by water for a given pore size. Another reason is attributed to the absence of oil slippage when the water phase exists between the oil phase and solid substrate even though water slippage appears instead.

Fig. 3b–d presents the water-oil flow profiles in pores with different sizes (50, 100 and 500 nm) to measure the impacts of water films on flow behavior when the pore size changes. Along with an expansion of the pore dimension, the oil flow capacity increases no matter whether a water film exists or not. According to

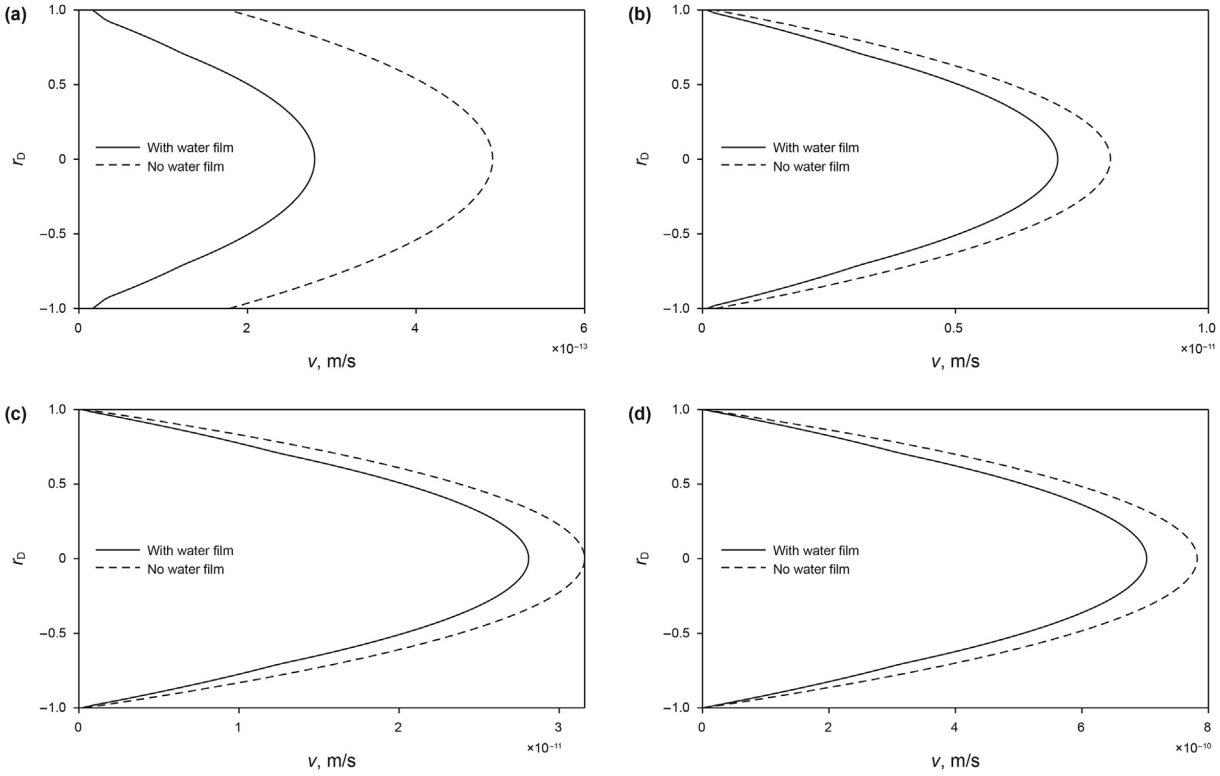

Fig. 3. Water-oil two phase flow profiles in wet and dry conditions in different-sized pores (θ=81.1°, $S_w = 0.5$, $\omega = 0.577$): (**a**) pore radius is 10 nm; (**b**) pore radius is 50 nm; (**c**) pore radius is 100 nm; (**d**) pore radius is 500 nm.

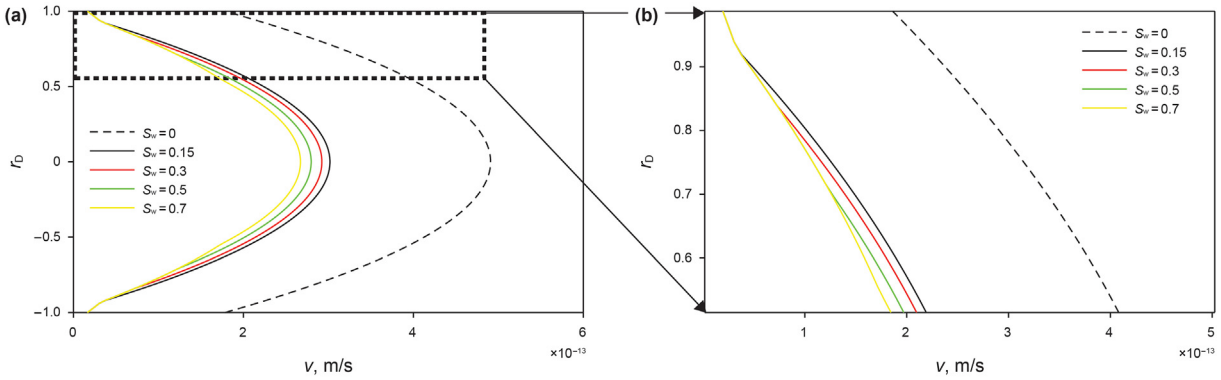

Fig. 5. Water-oil two-phase flow profiles in wet and dry conditions under different water saturations (r=10 nm, $\theta = 81.1°$, $\omega = 0.577$): (**a**) full plot; (**b**) local plot.

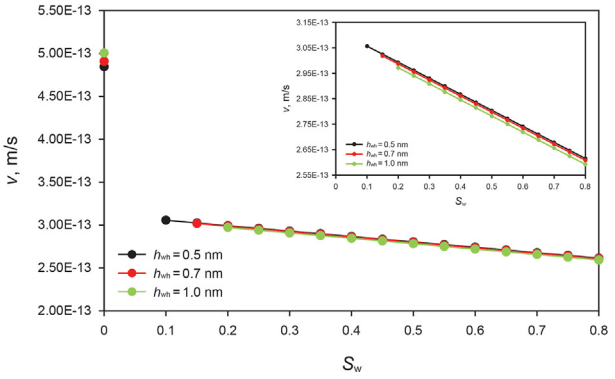

Fig. 6. Relationship between the maximum oil flow velocities and water saturation (r=10 nm, $\theta = 81.1°$, $\omega = 0.577$).

Fig. 4, the impacts of water is more significant in smaller pores when the water saturation is determined, especially when a pore radius is less than 30 nm as the relative difference is larger than 20% and it increases logarithmically after reaching 30 nm.

4.1.2. Water saturation

The impact of water content on two-phase flow behavior is also analyzed. An increase in water saturation tends to undermine the oil flow capacity for a fixed pore size according to Fig. 5, which shows oil flow patterns under different water saturations (0, 0.15, 0.3, 0.5 and 0.7). It is quite obvious that increasing water content leads to a drop in the oil flow capacity, as shown in Fig. 5a. Fig. 5b plots the flow details in the vicinities of the two interfaces. Besides the mentioned inflection point at the water-oil interface, there is another turning point between two water films as the water viscosity changes and the water movement speeds are different

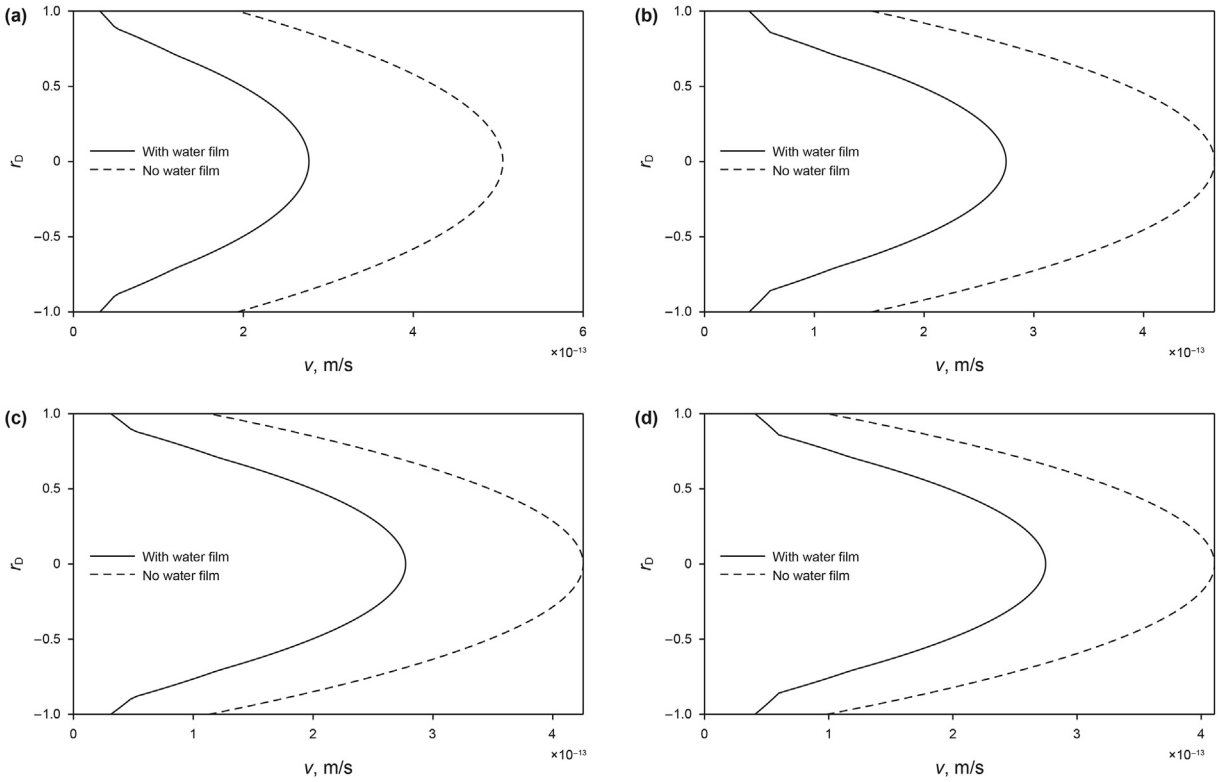

Fig. 7. Water-oil two-phase flow profiles in wet and dry conditions in nanopores with different hydrophilicity (r=10 nm, $S_w = 0.5$): (**a**) area ratio is 0.577; (**b**) area ratio is 0.7; (**c**) area ratio is 0.8; (**d**) area ratio is 0.9.

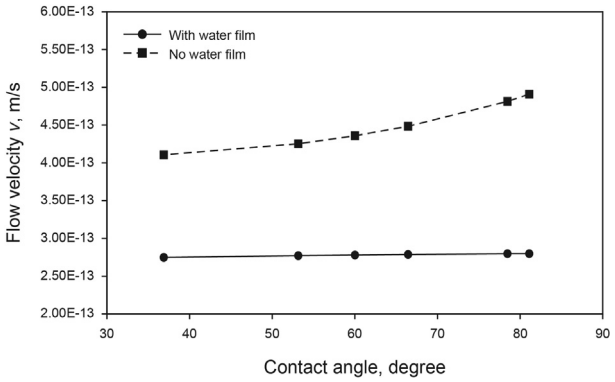

Fig. 8. Relationship between the maximum oil flow velocities and contact angle (r=10 nm, S_w = 0.5).

consequently. As the high-viscosity water film thickness is kept constant to be 0.7 nm in this study, these turning points overlap for the four listed wet cases while the inflection points at the water-oil interface are different because the bulk water film thickness changes with water saturation.

To be more precise, Fig. 6 illustrates a relationship between the maximum oil flow velocity and the water saturation, which proves that the existence of water reduces the oil flow capacity as the water phase occupies a certain flow sectional area. Increasing water saturation from 0 to 0.15 reduces the maximum oil flow velocity from 4.9087 $\times$ 10^{-13} m/s to 3.0182 $\times$ 10^{-13} m/s when the high-viscosity water film is 0.7 nm. Once the water saturation is larger than 0, there is a linear decline trend for the relationship between the maximum oil flow velocity and water saturation. As it is assumed that the high-viscosity water film thickness is kept constant to be 0.7 nm, the minimum water saturation is calculated to be 0.15 for the 10 nm pore. Fig. 6 also shows the relationship between the maximum oil flow velocities and water saturation when the high-viscosity water film is changed to 0.5 nm and 1.0 nm. A thicker high-viscosity water film reduces oil flow capacity due to the reduction of flow area. However, it also implies a more water-wet solid surface, which promotes oil flow in the dry condition and the maximum oil velocity reaches 4.8470 $\times$ 10^{-13}, 4.9087 $\times$ 10^{-13}, and 5.0049 $\times$ 10^{-13} m/s, respectively.

4.1.3. Area ratio

An area ratio is changed in this part to obtain water-oil two phase flow profiles when the hydrophilicity of substrate is adjusted. The shale nanopores discussed in this study are mainly inorganic pores which are usually hydrophilic. According to Appendix, changing the area ratio to 0.7, 0.8 and 0.9 (from 0.577) leads to the adhesion work to be 0.121, 0.136, and 0.150 J/m^2 (from 0.103 J/m^2) and the contact angle to be 66°, 53° and 36° (from 81.1°), respectively.

The effect of surface wettability on water and oil movements in nanopores is plotted in Fig. 7. The dash lines show that increasing hydrophilicity decreases the oil flow capacity due to a drop in the oil slip velocity, which is consistent with the results of Cui (2019). The solid lines also present that the smaller the contact angle, the smaller the maximum oil flow velocity. But the deline trend is quite slight and the reason goes to a reduction in water slippage. In order to describe the phenomenon more accurately, Fig. 8 provides a relationship between the maximum oil flow velocity and rock wettability quantatitively, which shows that the oil flow capacity

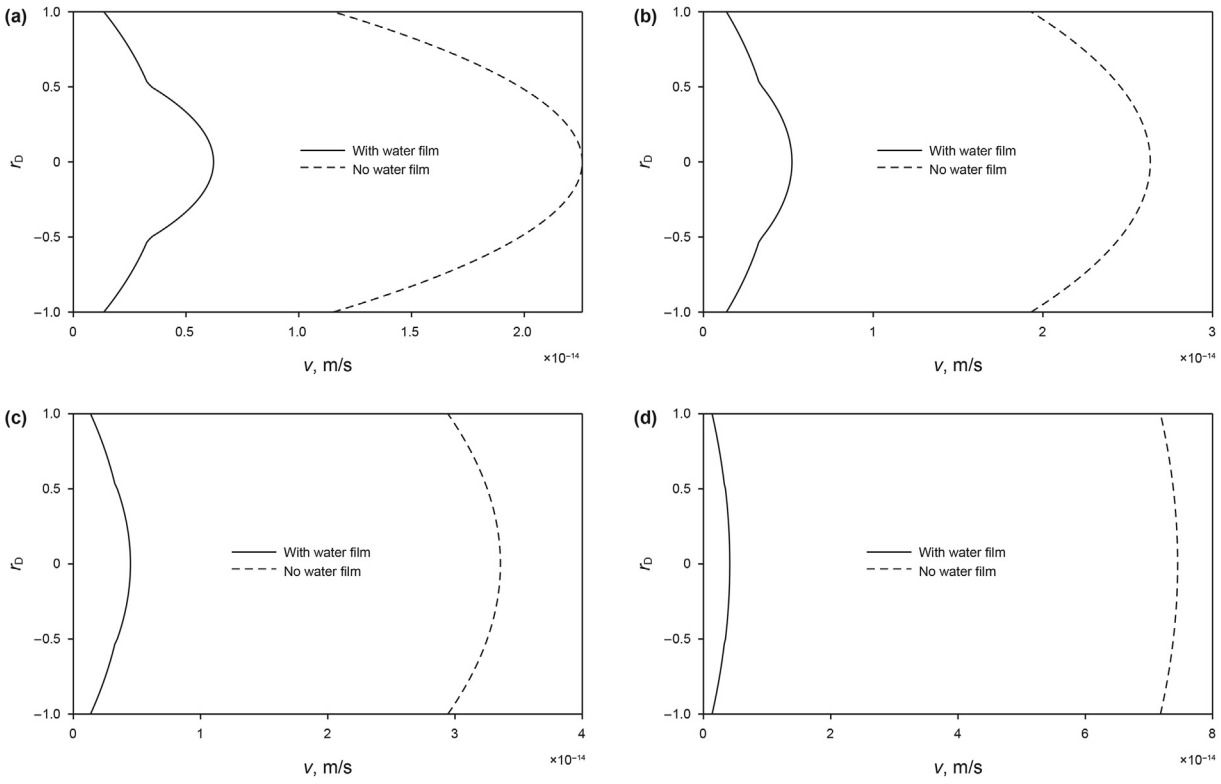

Fig. 9. Water-oil two-phase flow profiles in wet and dry conditions in nanopores when oil properties are different (r=1.5 nm, S_w = 0.75). (**a**) C_8H_{18}; (**b**) $C_{10}H_{22}$; (**c**) $C_{12}H_{26}$; (**d**) $C_{14}H_{30}$.

declines with an increase in surface hydrophilicity as it restricts water movement and impacts oil flow consequently.

4.1.4. Oil properties

As the required data for different *n*-alkanes in water-wet nanopores is limited, the single oil flow data from Wu et al. (2019) is adopted to illustrate the impacts of carbon number. They presented a variety of *n*-alkanes flow properties in organic nanopores. The pore radius is 1.5 nm in their study and the water saturation is improved to 0.75 to guarantee the existence of two water films in this section.

Figs. 9 and 10 show that the maximum oil flow velocity in a wet condition drops when the carbon number is larger as a result of more viscous oil phase. For example, increasing the carbon number from 8 to 14 results in the oil flow velocity at the center to be changed from 6.2187×10^{-15} m/s to 4.1328×10^{-15} m/s. However, the oil flow velocity in a dry condition becomes larger due to a larger oil slip velocity, which increases the maximum oil velocity from 2.2571×10^{-14} m/s to 7.4509×10^{-14} m/s. Therefore, the deviation of the oil flow capacities turns to be more significant.

4.2. Relative permeability curve

4.2.1. Pore size

Fig. 11 illustrates the evolution of relative permeability along

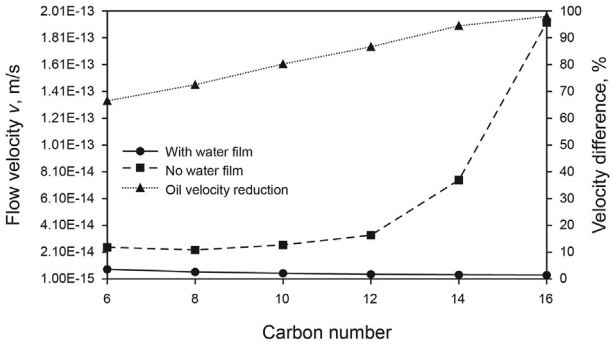

Fig. 10. Relationship between the maximum oil flow velocities and carbon number (r=1.5 nm, S_w = 0.75).

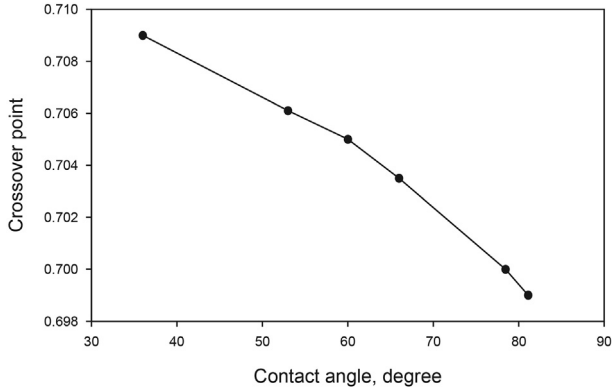

Fig. 13. Relationship between crossover point and pore wettability (r_{cmax}=100 nm).

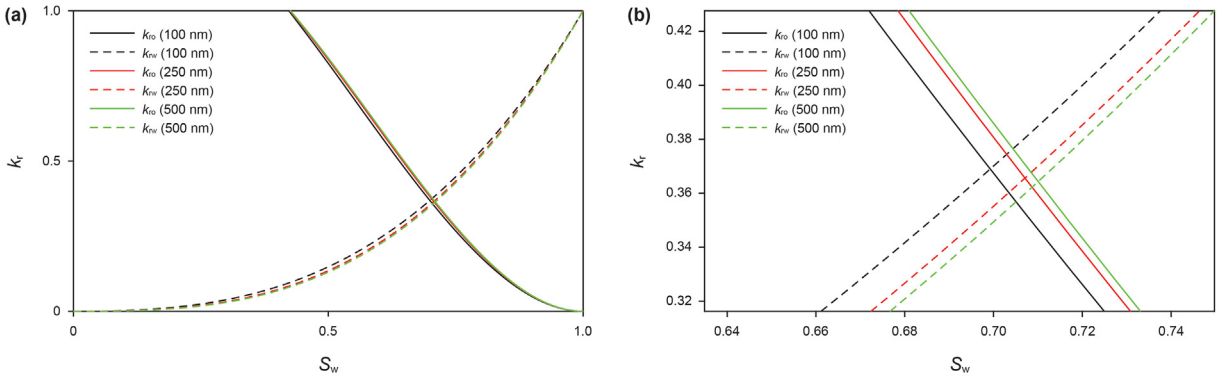

Fig. 11. Relationship between relative permeability curves and pore size (θ=81.1°, ω = 0.577): (**a**) full plot; (**b**) local plot.

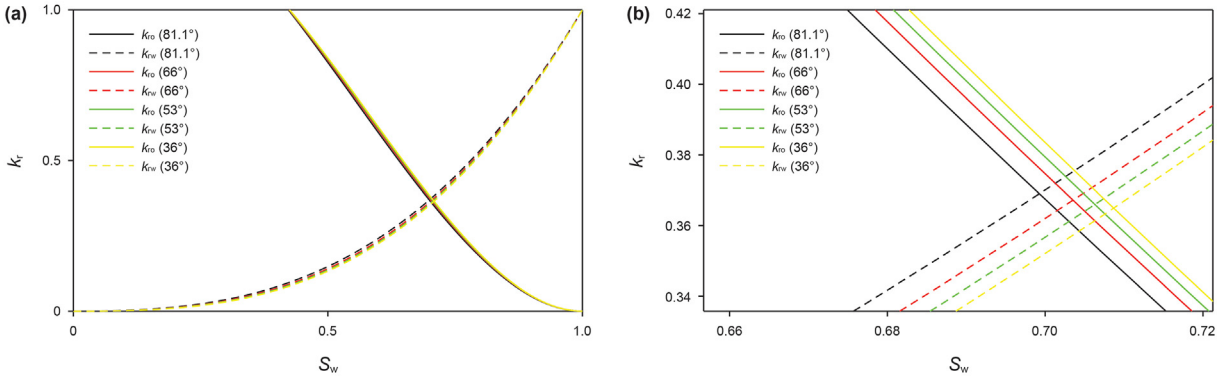

Fig. 12. Relationship between relative permeability curves and pore size (r_{cmax}=100 nm): (**a**) full plot; (**b**) local plot.

Table 1
Summary of validation parameters.

Parameter	Value	Approach to obtain the parameter
Pressure P	0.1 MPa	Measured with gauge
Temperature T	333.15 K	Measured with thermometer
Water viscosity μ_{w0}	1×10^{-3} Pa s	Measured with rotational viscometer
Oil viscosity μ_o	6.5×10^{-4} Pa s	Measured with rotational viscometer
Work of adhesion W_A	0.097 J/m^2	Obtained via Mattia and Calabrò (2012)
Surface diffusion coeffcient D	8.97×10^{-10} m^2/s	Obtained via Mattia and Calabrò (2012)
Average pore radius r	2.7×10^{-9} m	Measured with PSD test (nitrogen adsorption)
Pore length L	2.0×10^{-6} m	Obtained with average length from digital rock of core samples
High-viscosity water film thickness h_{wh}	7.0×10^{-10} m	Obtained via numerous MD simulations (Mashl et al., 2003; Neek-Amal et al., 2016)

Table 2
MSE between derived model and experimental data.

Dataset	MSE	
	K_{ro}	K_{rw}
Yu et al. (2014)	0.0233	0.0138
Wantawin et al. (2017)	0.0095	0.0143
Bo et al. (2019)	0.1400	0.0036

with the increase of the maximum radii, which are 100, 250, and 500 nm separately. The expansion of flow radius leads to a drop in the water slippage and a consequent smaller relative flow capacity of water phase. The crossover point moves slightly towards a higher water saturation from 0.699 to 0.707 and 0.710.

4.2.2. Area ratio

As previously illustrated, increasing the area ratio from 0.577 to 0.7, 0.8 and 0.9 modifies the contact angle. How water and oil phase flow in tubes with different wettability are shown in Fig. 12. Decreasing contact angle from 81.1° to 66°, 53° and 36° brings about a lower water flow capacity as a more water-wet solid surface restrains water movement to a larger extent. Fig. 13 provides the relationship between crossover point and pore wettability to present the impact more accurately.

5. Conclusions

This study calculates the confined water-oil two-phase flow capacity and water-oil relative permeability curves in inorganic nanopores in shale oil reservoirs with the consideration of different flow mechanisms. Oil slippage at a solid-oil surface is introduced in a dry condition while water slippage is considered in a wet condition. Different from the single oil phase flow model, this model describes how oil phase distributes and moves in the wet condition considering the impacts of solid properties, which better predicts the oil flow capacity in actual reservoir conditions. Assuming the log-normal pore size distribution, water-oil relative permeability curves are also obtained to enhance shale oil recovery. To be more precise, the following conclusions are obtained:

(1) The flow profiles under the two circumstances are compared to demonstrate the impacts of water content on the confined oil flow capacity. It is shown that oil flow profiles present a parabolic shape both in a dry condition and a wet condition and the existence of water reduces the oil flow capacity significantly by 42.97% at the center.
(2) A larger pore dimension brings about a larger oil flow velocity regardless of the water content. The effect of water is more significant in smaller pores, especially when the pore radius is less than 30 nm.
(3) The maximum oil flow velocity decreases linearly with an increase in water saturation in the wet condition. Increasing water saturation from 0 to 0.15 reduces the maximum oil flow velocity by 38.51%.
(4) Increasing the surface hydrophilicity decreases the oil flow capacity due to a smaller oil slip velocity in the dry condition. Similarly, the maximum oil flow velocity in the wet condition drops given a smaller contact angle because of a reduction in water slippage.
(5) The maximum oil flow velocity in the wet condition drops when the carbon number is larger as a result of a larger oil viscosity. Increasing the carbon number from 8 to 14 results in 33.54% decline in oil flow velocity at the center. In contrast, the oil flow velocity in the dry condition becomes larger due to an increase in the oil slip velocity.
(6) Due to a drop in water slippage, the crossover point moves slightly given a larger pore structure.
(7) Increasing the inorganic to organic surface area ratio restrains water movement to a larger extent.

This paper mainly works to investigate the analytical modelling of steady-state shale oil flow in the wet condition, which doesn't consider the rock heterogeneity and complicated pore structure.

Table 3
Basic parameters used in results and discussion.

Parameter	Value
Pressure[1] P	0.1 MPa
Temperature[1] T	293.15 K
Water viscosity μ_{w0}	1×10^{-3} Pa s
Oil viscosity[1] μ_o	8×10^{-4} Pa s
Work of adhesion[2] W_A	0.103 J/m^2
Work of adhesion (oil-wet)[2] W_{Ao}	0.019 J/m^2
Work of adhesion (water-wet)[2] W_{Aw}	0.165 J/m^2
Surface diffusion coeffcient[1] D	8.354×10^{-10} m^2/s
Surface diffusion coeffcient (oil-wet)[1] D_o	3×10^{-9} m^2/s
Surface diffusion coeffcient (water-wet)[1] D_w	3×10^{-10} m^2/s
Average pore radius[1] r	10 nm
Pore length[1] L	2×10^{-6} m
High-viscosity water film thickness h_{wh}	7×10^{-9} m
Contact angle, degree	81.1
Viscosity ratio[3] C	2.1
Carbon number[1]	10
Area ratio[2] ω	0.577
Water saturation S_w	0.5

Note: 1. Cui (2019); 2. Mattia and Calabrò (2012); 3. Qin and Buehler (2015).

Pore-scale modelling of multiphase flow on digital rocks with the consideration of slippage will be investigated in the future study. Molecular simulation will also be conducted to further validate the two-phase flow pattern.

Acknowledgements

The authors would like to acknowledge the NSERC/Energi Simulation and Alberta Innovates Chairs for providing research funding. Keliu Wu would like to acknowledge the Beijing Natural Science Foundation (2204093) and Science Foundation of China University of Petroleum, Beijing (No. 2462018YJRC033) for providing research funding.

Appendix

In this study, basic data such as P, T, μ_o, r and L are chosen according to Cui (2019). Also, Cui (2019) discussed the effect of mixed wettability on single oil phase flow in shale nanopores. They calculated the mixed adhesion work and mixed surface diffusion coeffcient based on the area ratio ω (ω is the water-wet surface area ratio and $1-\omega$ is the oil-wet surface area ratio) by arithmetic average and statistic average (Eqs. (A-1) and (A-2)). However, only the values for D_o and D_w come from Cui (2019). The values for W_A and θ are obtained from Mattia and Calabrò (2012) and they also provided the relationship between W_A and θ (Eq. (A-3)). Then W_{Ao} and W_{Aw} are obtained with Eq. (A-3) by adjusting contact angle θ, which can be obtained with Eq. (A-4) (Tao et al., 2018). Finally, ω is further calculated based on Eq. (A-1) and D can be figured out by following Eq. (A-2).

$$W_A = (1-\omega)W_{Ao} + \omega W_{Aw} \tag{A-1}$$

$$D = \sqrt{\frac{(1-\omega)D_o + \omega D_w}{\frac{\omega}{D_w} + \frac{1-\omega}{D_o}}} \tag{A-2}$$

$$W_A = \pi_e + \sigma_{lv}(1 + cos\theta) \tag{A-3}$$

$$\theta = \arccos(-1.48 + 17.45\varepsilon_{sw}) \tag{A-4}$$

where W_{Ao} and W_{Aw} are adhesion works of pure oil-wet substrate and pure water-wet substrate, respectively, J/m^2; D_o and D_w are surface diffusion coefficients of pure oil-wet substrate and pure water-wet substrate, respectively, m^2/s; π_e is the spreading pressure, J/m^2; σ_{lv} is the liquid-vapor surface tension, N/m; ε_{sw} is the Lennard-Jones energy parameter between solid atom and water atom. When ε_{sw} is 391.99896 J/mol, θ is 81.1°.

References

Afsharpoor, A., Javadpour, F., 2016. Liquid slip flow in a network of shale noncircular nanopores. Fuel 180, 580–590. https://doi.org/10.1016/j.fuel.2016.04.078.
Afsharpoor, A., Javadpour, F., 2018. Pore connectivity between organic and inorganic matter in shale: network modeling of mercury capillary pressure. Transport Porous Media 25 (3), 503–519. https://doi.org/10.1007/s11242-018-1132-0.
Barrat, J.L., Bocquet, L., 1999. Large slip effect at a nonwetting fluid-solid interface. Phys. Rev. Lett. 82 (23), 4671. https://doi.org/10.1103/PhysRevLett.82.4671.
Blake, T.D., 1990. Slip between a liquid and a solid: DM Tolstoi's (1952) theory reconsidered. Colloids Surf., A 47, 135–145. https://doi.org/10.1016/0166-6622(90)80068-F.
Bo, L., Song, F., Zhang, S., 2019. Analysis of test method for oil and water relative permeability curve in tight reservoirs. IOP Conf. Ser. Earth Environ. Sci. 332 (2), 022019. https://doi.org/10.1088/1755-1315/332/2/022019.
Cane, R.F., 1976. The Origin and Formation of Oil Shale. Oil Shale. Elsevier, Amsterdam, pp. 27–60.
Cantisano, M.T., Restrepo, D.P., Cespedes, S., Toelke, J., Grader, A., Suhrer, M., Walls, J., 2013. Relative permeability in a shale formation in Colombia using digital rock physics. SPE/AAPG/SEG Unconventional Resources Technology Conference, Denver, Colorado, USA. https://doi.org/10.1190/urtec2013-092.
Chalmers, G.R., Bustin, R.M., Power, I.M., 2012. Characterization of gas shale pore systems by porosimetry, pycnometry, surface area, and field emission scanning electron microscopy/transmission electron microscopy image analyses: examples from the Barnett, Woodford, Haynesville, Marcellus, and Doig units. AAPG Bull. 96 (6), 1099–1119. https://doi.org/10.1306/10171111052.
Chen, Z., Huan, G., Ma, Y., 2006. Computational Methods for Multiphase Flows in Porous Media. Computational Science and Engineering Series, SIAM, Philadelphia.
CMG, 2017. User's Guide IMEX Advanced Oil/Gas Reservoir Simulator. Computer Modelling Group.
Cui, J., 2019. Oil transport in shale nanopores and micro-fractures: modeling and analysis. J. Petrol. Sci. Eng. 178, 640–648. https://doi.org/10.1016/j.petrol.2019.03.088.
Cui, J., Sang, Q., Li, Y., Yin, C., Li, Y., Dong, M., 2017. Liquid permeability of organic nanopores in shale: calculation and analysis. Fuel 202, 426–434. https://doi.org/10.1016/j.fuel.2017.04.057.
Curtis, M.E., Ambrose, R.J., Sondergeld, C.H., Rai, C.S., 2011. Investigation of the relationship between organic porosity and thermal maturity in the Marcellus Shale. In: SPE North American Unconventional Gas Conference and Exhibition, The Woodlands, Texas, USA. https://doi.org/10.2118/144370-MS.
Darabi, H., Ettehad, A., Javadpour, F., Sepehrnoori, K., 2012. Gas flow in ultra-tight shale strata. J. Fluid Mech. 710, 641–658. https://doi.org/10.1017/jfm.2012.424.
Dembicki, H., 2016. Practical Petroleum Geochemistry for Exploration and Production. Elsevier.
Fekete, F.A.S.T., 2017. Well Test User Manual. Fekete Associates. Inc.
Gao, Z., Fan, Y., Hu, Q., Jiang, Z., Cheng, Y., Xuan, Q., 2019. A review of shale wettability characterization using spontaneous imbibition experiments. Mar. Petrol. Geol. 109, 330–338. https://doi.org/10.1016/j.marpetgeo.2019.06.035.
Gupta, I., Jernigen, J., Curtis, M., Rai, C., Sondergeld, C., 2018. Water-wet or oil-wet: is it really that simple in shales? Petrophysics 59 (3), 308–317. https://doi.org/10.30632/PJV59N3-2018a2.
Holt, J.K., Park, H.G., Wang, Y., Stadermann, M., Artyukhin, A.B., Grigoropoulos, C.P., Noy, A., Bakajin, O., 2006. Fast mass transport through sub-2-nanometer carbon nanotubes. Science 312 (5776), 1034–1037. https://doi.org/10.1126/science.1126298.
Huang, J., Jin, T., Chai, Z., Barrufet, M., Killough, J., 2020. Compositional simulation of three-phase flow in mixed-wet shale oil reservoir. Fuel 260, 116361. https://doi.org/10.1016/j.fuel.2019.116361.
Jin, Z., Firoozabadi, A., 2016. Thermodynamic modeling of phase behavior in shale media. SPE J. 21 (1), 190–207. https://doi.org/10.2118/176015-PA.
Li, T., Song, H., Wang, J., Wang, Y., Killough, J., 2016. An analytical method for modeling and analysis gas-water relative permeability in nanoscale pores with interfacial effects. Int. J. Coal Geol. 159, 71–81. https://doi.org/10.1016/j.coal.2016.03.018.
Li, R., Wu, K., Li, J., Xu, J., Chen, Z., 2018. Gas transport in shale nanopores with mobile high-viscosity water film. Ind. Eng. Chem. Res. 57 (32), 11219–11228. https://doi.org/10.1021/acs.iecr.8b02363.
Li, R., Wu, K., Li, J., Xu, J., Chen, Z., 2019. Shale gas transport in wedged nanopores with water films. J. Nat. Gas Sci. Eng. 66, 217–232. https://doi.org/10.1016/j.jngse.2019.04.001.
Loucks, R.G., Reed, R.M., Ruppel, S.C., Jarvie, D.M., 2009. Morphology, genesis, and distribution of nanometer-scale pores in siliceous mudstones of the Mississippian Barnett Shale. J. Sediment. Res. 79, 848–861. https://doi.org/10.2110/jsr.2009.092.
Mashl, R.J., Joseph, S., Aluru, N.R., Jakobsson, E., 2003. Anomalously immobilized water: a new water phase induced by confinement in nanotubes. Nano Lett. 3 (5), 589–592. https://doi.org/10.1021/nl0340226.
Mattia, D., Calabrò, F., 2012. Explaining high flow rate of water in carbon nanotubes via solid–liquid molecular interactions. Microfluid. Nanofluidics 13 (1), 125–130. https://doi.org/10.1007/s10404-012-0949-z.
Myers, T.G., 2011. Why are slip lengths so large in carbon nanotubes? Microfluid. Nanofluidics 10 (5), 1141–1145. https://doi.org/10.1021/nl0340226.
Navier, C.L.M.H., 1823. Mémoire sur les lois du mouvement des fluides. Mém. Acad. Sci. Inst.de France. 6, 389–440.
Neek-Amal, M., Peeters, F.M., Grigorieva, I.V., Geim, A.K., 2016. Commensurability effects in viscosity of nanoconfined water. ACS Nano 10 (3), 3685–3692. https://doi.org/10.1021/acsnano.6b00187.
Odusina, E.O., Sondergeld, C.H., Rai, C.S., 2011. NMR study of shale wettability. In: SPE Canadian Unconventional Resources Conference. https://doi.org/10.2118/147371-MS. Calgary, Alberta, Canada.
Ojha, S.P., Misra, S., Tinni, A., Sondergeld, C., Rai, C., 2017. Relative permeability estimates for Wolfcamp and Eagle Ford shale samples from oil, gas and condensate windows using adsorption-desorption measurements. Fuel 208, 52–64. https://doi.org/10.1016/j.fuel.2017.07.003.
Passey, Q.R., Bohacs, K., Esch, W.L., Klimentidis, R., Sinha, S., 2010. From oil-prone source rock to gas-producing shale reservoir-geologic and petrophysical characterization of unconventional shale gas reservoirs. In: SPE International Oil and Gas Conference and Exhibition in China, Beijing, China. https://doi.org/10.2118/131350-MS.
Qin, Z., Buehler, M.J., 2015. Nonlinear viscous water at nanoporous two-dimensional interfaces resists high-speed flow through cooperativity. Nano Lett. 15 (6), 3939–3944. https://doi.org/10.1021/acs.nanolett.5b00809.
Rouquerol, J., Avnir, D., Fairbridge, C.W., Everett, D.H., Haynes, J.M., Pernicone, N., Ramsay, J.D.F., Sing, K.S.W., Unger, K.K., 1994. Recommendations for the

characterization of porous solids (Technical Report). Pure Appl. Chem. 66 (8), 1739–1758. https://doi.org/10.1351/pac199466081739.
Ruckenstein, E., Rajora, P., 1983. On the no-slip boundary condition of hydrodynamics. J. Colloid Interface Sci. 96 (2), 488–491. https://doi.org/10.1016/0021-9797(83)90050-4.
Saraji, S., Piri, M., 2015. The representative sample size in shale oil rocks and nano-scale characterization of transport properties. Int. J. Coal Geol. 146, 42–54. https://doi.org/10.1016/j.coal.2015.04.005.
Siddiqui, M.A.Q., Ali, S., Fei, H., Roshan, H., 2018. Current understanding of shale wettability: a review on contact angle measurements. Earth Sci. Rev. 181, 1–11. https://doi.org/10.1016/j.earscirev.2018.04.002.
Sun, F., Yao, Y., Li, G., Zhang, S., Xu, Z., Shi, Y., Li, X., 2019. A slip-flow model for oil transport in organic nanopores. J. Petrol. Sci. Eng. 172, 139–148. https://doi.org/10.1016/j.petrol.2018.09.045.
Tao, J., Song, X., Zhao, T., Zhao, S., Liu, H., 2018. Confinement effect on water transport in CNT membranes. Chem. Eng. Sci. 192, 1252–1259. https://doi.org/10.1016/j.ces.2018.05.018.
Wang, S., Javadpour, F., Feng, Q., 2016a. Molecular dynamics simulations of oil transport through inorganic nanopores in shale. Fuel 171, 74–86. https://doi.org/10.1016/j.fuel.2015.12.071.
Wang, S., Javadpour, F., Feng, Q., 2016b. Fast mass transport of oil and supercritical carbon dioxide through organic nanopores in shale. Fuel 181, 741–758. https://doi.org/10.1016/j.fuel.2016.05.057.
Wantawin, M., Yu, W., Sepehrnoori, K., 2017. An iterative work flow for history matching by use of design of experiment, response-surface methodology, and Markov chain Monte Carlo algorithm applied to tight oil reservoirs. SPE Reservoir Eng. 20 (3), 613–626. https://doi.org/10.2118/185181-PA.
Wu, K., Chen, Z., Li, J., Lei, Z., Xu, J., Wang, K., Li, R., Dong, X., Peng, Y., Yang, S., Zhang, F., 2019. Nanoconfinement effect on *n*-alkane flow. J. Phys. Chem. C 123 (26), 16456–16461. https://doi.org/10.1021/acs.jpcc.9b03903.
Youngquist, W., 1998. Shale oil—The elusive energy, 98. Hubbert Center Newsletter, pp. 1–7, 4.
Yu, W., Lashgari, H., Sepehrnoori, K., 2014. Simulation study of CO_2 huff-n-puff process in Bakken tight oil reservoirs. SPE Western North American and rocky mountain joint meeting, Denver, Colorado. https://doi.org/10.2118/169575-MS.
Zhang, T., Li, X., Sun, Z., Feng, D., Miao, Y., Li, P., Zhang, Z., 2017a. An analytical model for relative permeability in water-wet nanoporous media. Chem. Eng. Sci. 174, 1–12. https://doi.org/10.1016/j.ces.2017.08.023.
Zhang, Q., Su, Y., Wang, W., Lu, M., Sheng, G., 2017b. Apparent permeability for liquid transport in nanopores of shale reservoirs: coupling flow enhancement and near wall flow. Int. J. Heat Mass Tran. 115, 224–234. https://doi.org/10.1016/j.ijheatmasstransfer.2017.08.024.
Zou, C., 2017. Unconventional Petroleum Geology. Elsevier.